Nuclear Instruments and Methods in Physics Research A 1059 (2024) 168998

Contents lists available at ScienceDirect

Nuclear Inst. and Methods in Physics Research, A

journal homepage: www.elsevier.com/locate/nima

On planar (110) channeling of 500 MeV positrons and electrons in silicon semiconductor detectors

H. Backe

Institute for Nuclear Physics of Johannes Gutenberg-University, Johann-Joachim-Becher-Weg 45, Mainz, D-55128, Germany

ARTICLE INFO

Keywords:
Crystalline undulator
Channeling of positrons and electrons
Computer simulation calculations
Role of plasmon resonances
Energy loss in silicon detectors
Spectral power density analysis

ABSTRACT

The investigation of the channeling phenomenon of positrons in single crystals relies on the availability of high quality positron beams. At the Mainz Microtron MAMI a facility is under construction which will supply a 500 MeV positron beam (Backe et al., 2022) with an emittance of $\epsilon_v = 0.055\ \pi$ mm mrad (1 σ) in vertical direction. The beam line allows focusing of the positron beam in the target chamber with an angular spread of 64 μrad (FWHM) at a beam width of 5 mm (FWHM). Employing a silicon detector oriented in (110) channeling conditions, it is intended to measure in a triple coincidence the energy loss of the positrons in the silicon detector, as proposed in a recent paper by Shchagin et al. (2022), the scattering angle and the energy of the emitted photons. In this paper a case study is presented with the aid of simulation calculations for such an experiment with special emphasis on the role of the plasmon resonances in silicon at 17 and 3.9 eV. Simulation results are presented for an electron beam of 500 MeV from MAMI as well.

1. Introduction

It is well known that at passage of an ultra-relativistic positrons or electrons through condensed matter, the lepton may suffer scattering either at the screened Coulomb potential of an atomic nucleus or at bound or free electrons. As introduced by Lindhard [1], in single crystals atomic planes form potential walls with depths in the order of tenth of eV in which the lepton may be captured. At a scattering process the transverse energy changes resulting eventually in a de-channeling process. For the calculation of the excitation energy and the energy loss as function of the longitudinal distance the particle moves in the crystal, the density of the atoms and electrons as well as differential cross-sections are required as function of the transverse coordinate across the channel. Various simulation codes were developed by a number of authors, for an overview see, e.g., Korol et al. [2, Chapter 2]. The formalism applied in this paper is based on the continuum potential picture, as others of e.g. Bagli and Guidi [3] and Sytov et al. [4] as well, and was described in two recent publications in detail [5,6].

The change of the transverse energy is dominated by the electron-atom scattering. The interaction with electrons is only a small correction. For the electron density a uniform distribution was assumed in [5,6] which is a rather good approximation. However, for positron channeling the situation turns out to be more complicated (see Fig. 3 below). The reason is that for deeply transversely bound positrons in the channeling potential, the positron–electron interaction is the dominating one. As a consequence, the knowledge of the positron–electron cross-section and the electron density distribution across the channel is of crucial importance.

In this paper a more refined model has been developed to describe the positron–electron interaction. It is also based on the relativistic extended Ashley model which describes the double differential cross-section as function of the momentum transfer q and the energy transfer W to an electron. From these quantities the scattering angle distribution and the energy loss can be calculated. It turns out that the double differential cross-section must be separated into a distant collision part which contains the strong low energy plasmon excitations, and a close collision part which describes K- and L-inner shell excitations with delta ray production.

The above outlined scheme has been applied for the calculation of the energy deposited into the sensitive layer of a silicon detector, aligned for (110) channeling, resulting in the characteristic energy loss (Landau) distribution. For an overview of this field see the recent publication of Shchagin et al. [7]. Our experiment will be performed with 500 MeV positrons from the positron beam line at the Mainz Microtron MAMI [8]. The experimental set-up will allow to measure triple coincidences of the energy loss of the positrons in the silicon detector, the scattering angle, and the energy of the emitted photons. The question will be addressed which additional information of the channeling process can be extracted from special conditions selected by gates on the recorded triple coincidence distributions.

E-mail address: backe@uni-mainz.de.

https://doi.org/10.1016/j.nima.2023.168998
Received 29 September 2023; Received in revised form 1 December 2023; Accepted 4 December 2023
Available online 5 December 2023

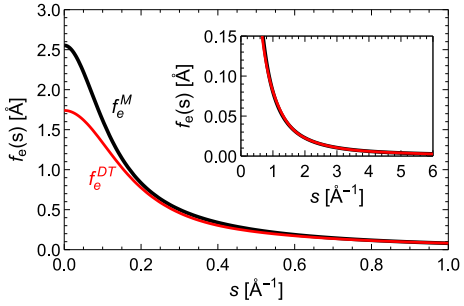

Fig. 1. Positron scattering factors for atomic silicon. The black full curve f_e^M represents the Molière approximation [9] with the original parameter set, the red one f_e^{DT} that of Doyle and Turner [11] in a six-parameter representation [10].

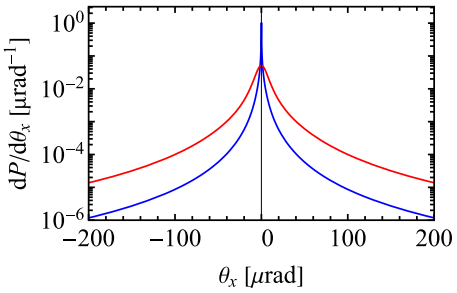

Fig. 2. Normalized lepton-atom (red) and lepton-electron (blue) scattering distributions at 500 MeV. The FWHM amount to 13.7 μrad (atomic) and 0.096 μrad (electronic). Both distributions have long tails taken into account in the numerical simulation up to ± 0.033 rad. The root mean squared scattering angles amount to $\langle\theta_x^2\rangle^{1/2}$ = 38.3 μrad (atomic), and 12.3 μrad (electronic). The total scattering cross-sections are $\sigma_{tot}^{(at)}$ = 89.4· 10^{-4} Å^2 and $\sigma_{tot}^{(el)}$ = 5.17 ·10^{-4} Å^2, the mean transverse energy gains $\langle\Delta E_\perp/\Delta z\rangle_{at}$ = 1.64 eV/μm and $\langle\Delta E_\perp/\Delta z\rangle_{el}$ = 0.137 eV/μm, and the mean number of collisions 4.46/μm (atomic) and 3.62/μm (electronic), for the atomic and electronic contributions, respectively.

For comparison, some results of calculations for a 500 MeV electron beam will be presented as well.

2. Description of the model

For the calculation of the channeling potential, as well as the angular distribution of the scattered leptons, the Molière representation for the electronic scattering factors [9] has been utilized which holds in the Born approximation also for positrons. The parameters for silicon are

$$\alpha = \{0.514906,\ \ 0\ \ ,\ 0.485094\}$$
$$\beta = \{2.113681,\ 1.2,\ 0.41510\}/a_{TF}. \tag{1}$$

Here are a_{TF} = 0.8853 a_0 $Z^{-1/3}$ the Thomas–Fermi screening factor with a_0 the Bohr radius, and Z=14 for silicon. This parameter set approximates the six- parameter Doyle-Turner representation quoted by Chouffani and Überall [10] to better than 8% in the full range of $0 \le s/\text{Å} \le 6$, see Fig. 1. The quantity s is related to the momentum transfer by $q = 2pv/(\hbar c)\sin(\vartheta/2) = 4\pi s$, with p the momentum of the particle, v its velocity, c the speed of light, and ϑ the scattering angle. For further details see [5].

The normalized scattering distribution function for lepton-atom interaction at an energy of 500 MeV is

$$P_{500}^{(at)}(\theta_x) = \Big(\frac{4.87068\cdot10^{-10}+\theta_x^2}{(7.0885\cdot10^{-11}+\theta_x^2)^{3/2}} - \frac{1.36902\cdot10^{-9}+\theta_x^2}{(1.83793\cdot10^{-9}+\theta_x^2)^{3/2}}\Big)/15.5081, \tag{2}$$

with θ_x the projected scattering angle. The numerical parameters are related to the Molière parameters of Eq. (1). The distribution function is depicted in Fig. 2, red curve.

The potential $U(x)$ has been calculated according to chapter 9.1 of the textbook of Baier et al. [13]. The results for electron and positron channeling are shown in Fig. 3 together with positive $n_p(x)$ and negative $n_e(x)$ charge number densities across the channel. The latter has been derived from $U(x)$ with the aid of the one dimensional Poisson equation to be

$$n_e(x) = -\frac{U_0}{4\pi\alpha\hbar c}\frac{d^2U(x)/U_0}{dx^2} + n_p(x), \tag{3}$$
$$n_p(x) = \frac{A}{\sqrt{2\pi}u_1}\exp(-x^2/2u_1^2), \tag{4}$$

with u_1 = 0.0784 Å at 293 K [14], and A = 1.3425/Å^2. Quite remarkable differences can be recognized for electron and positron channeling. At electron channeling a strong overlap between the particle with the nuclear charge as well as the electron charge density exists. Since the electron-atom scattering distribution is much broader than the electron–electron one, the latter turns out to be a correction. This is

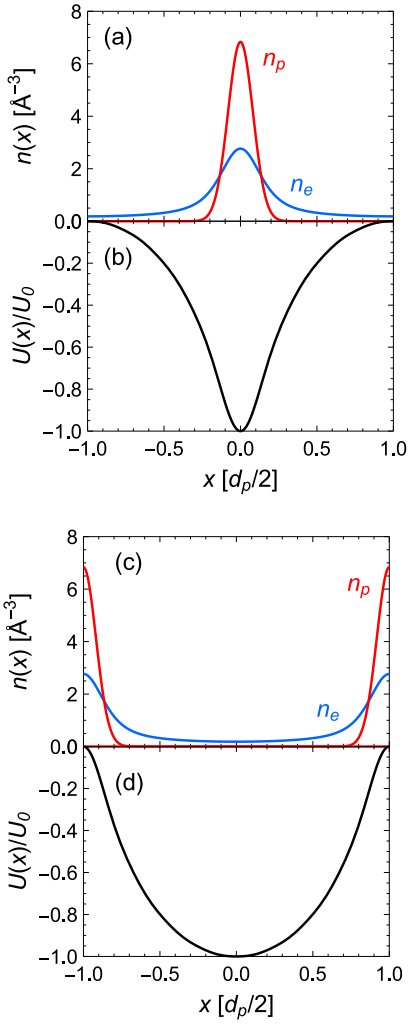

Fig. 3. Upper part: (a) Electron density $n_e(x)$, and density of positive charge $n_p(x)$ as function of the distance coordinate x across the planes. The inter-planar distance amounts to $d_p = \sqrt{2}a/4$ = 1.920 Å, with a = 5.431 Å the lattice constant of crystalline silicon at 300 K [12]. The quantity $(1/d_p)\int_{-d_p/2}^{d_p/2} n_e(x)dx = Z\cdot(8/a^3)$ = 0.699/Å^3 is the mean electron density for silicon with Z = 14. (b) Potential of the (110) plane for electron channeling normalized to the potential depth $|U_0|$ = 21.09 eV. Lower part: Same for positron channeling.

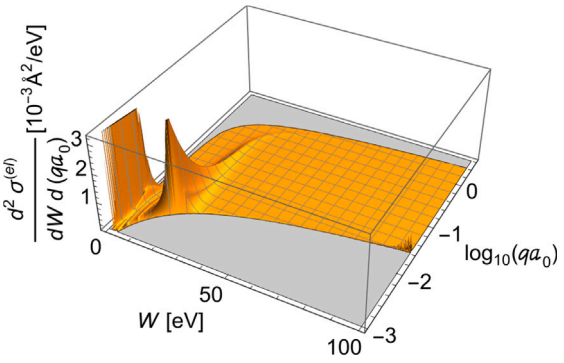

Fig. 4. Double differential cross-section for lepton-lepton interactions as function of the energy loss W and momentum transfer qa_0. The kinematical allowed region lifts clearly out from the gray area. Two dominating features are the plasmon resonance at $W = 17$ eV and $qa_0 \simeq 0.0045$, and the resonance of the transverse excitation at $W = 3.9$ eV and $qa_0 \simeq 0.0013$ which is some orders of magnitudes higher than shown.

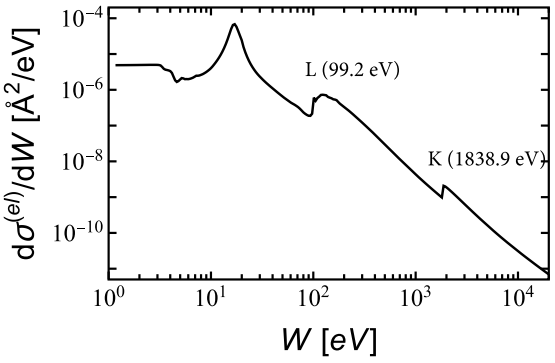

Fig. 5. Sum of longitudinal and transverse differential cross-sections as function of the energy loss, derived from Fig. 4.

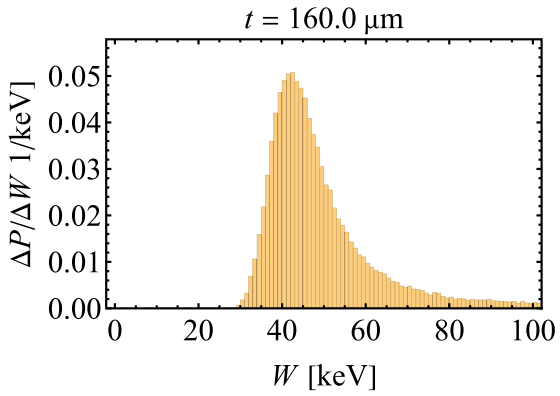

Fig. 6. Probability density for the energy loss distribution of a 160 µm thick silicon crystal in random orientation, i.e. amorphous matter.

not at all the case for positron channeling for which the positron–electron interaction dominates for transverse binding energies $E_\perp < -0.4\ U(x)/U_0$. This fact requires special considerations as described below.

3. Differential cross-sections for scattering at electrons

Let us turn to the discussion of the cross-section for the positron–electron scattering. The calculation will be performed with the Møller rather than the Bhabha representation since for a low energy transfer both cross-sections are essentially the same. Generally, the double differential cross-section $d^2\sigma/dW\,dq$ is a function of the momentum transfer q and the energy transfer W. For longitudinal excitations it has been derived from the complex dielectric function $\mathrm{Im}[-1/\epsilon(q,W)]$, which was extended from $q = 0$ by the relativistical extended model of Ashley [15, and references cited therein]. The quantity $\epsilon(q = 0, W)$ was constructed in the energy region 30.85 eV $\leq W <$ 30 keV from the Henke tables [16,17], and for 1.1 eV $\leq W <$ 30.85 eV from Bichsel data for the optical oscillator strength (OOS) [18]. The contribution of the transversal cross-section was calculated with the model of Fernández-Varea et al. [19] and added to the longitudinal cross-section. Further details were described in [5] for a diamond single crystal which have been applied mutatis mutandis for silicon. The low energy part of the double differential cross-section at scattering on atomic electrons is shown in Fig. 4.

The energy differential cross-sections as function of the energy loss W and momentum transfer qa_0, with a_0 the Bohr radius, are obtained after proper integration over the kinematical allowed qa_0 and the kinematical allowed W, respectively. The result is shown in Fig. 5. Qualitatively two domains can be distinguished: the resonance region below the binding energy of 100 eV for the L electrons, and the inner-shell excitation region above. To proceed further model assumptions were made. To be specific, (i) for the resonance region it was assumed that it has a sharp cut-off at the L-shell binding energy $E_L = 99.2$ eV, and (ii) the inner shell excitation above that energy has an upper limit at twice the K-shell binding energy of $E_K = 1838.9$ eV. Assumption (i) neglects a small part of the double differential cross-section above $\min[W_{low}(qa_0) + E_L, W_{high}(qa_0)]$, and (ii) truncates the double differential cross-section at $\min[W_{low}(qa_0)+2E_K, W_{high}(qa_0)]$ with $W_{low}(qa_0)$ and $W_{high}(qa_0)$ the limits of the kinematical allowed region, see Fig. 4. The implication of these approximations will be discussed below.

4. Test of the model

The reliability of the described model can be tested by different means. First of all, it was found that asymptotically the differential cross-sections merges into the Møller cross-sections for the interaction with free electrons, as required. Further quantities which can be compared with other references are the total electronic energy loss per collision with an electron, resulting in 2.044 MeV/(g/cm^2), which should be 2.046 MeV/(g/cm^2) [20], and the logarithmic mean excitation energy 162.3 eV, which should be 173.0 eV [21].

Although the electronic mean energy loss is predicted quite accurately by the model, simulation calculations impose restrictions at high energies due to lack of statistics. However, looking only to the region of the most probable energy loss, i.e. the Landau distribution, the mentioned restriction can be largely neglected. Fig. 6 shows a simulation result for a crystal with a thickness of 160 µm in random orientation.

This distribution can be compared with results obtained by H. Bichsel [18]. In TABLE V and VI of his review article the most probable energy loss Δ_p and the full width of half maximum (FWHM) w are tabulated for various thicknesses of the silicon absorber t. For a comparison the values $\Delta_p = 43.4$ keV and $w = 18.3$ keV at $t = 160$ µm are of relevance which agree with Fig. 6 within +1.8% and −8.2% for the most probable energy loss and the FWHM, respectively, i.e., the calculated Landau distribution of this work agrees well at the energy position but the width is somewhat narrower.

Also the K- and L-shell ionization cross-sections can be calculated with the model and compared with measurements of D.H.H. Hoffmann et al. [22]. For both, the K- and L- shell ionization, the E_0/I scale of the graph Fig. 13 [22] must be extrapolated far beyond the shown upper limit. It is doubtful, on the one hand, to compare the extracted value of the cross-sections $\sigma_K = 10 \cdot 10^{-6}$ Å^2 and $\sigma_L = 2.2 \cdot 10^{-4}$ Å^2 with the values obtained in this work which are $2.7 \cdot 10^{-6}$ Å^2 and $1.0 \cdot 10^{-4}$ Å^2 for K- and L-shell excitation, respectively. On the other hand, one can

doubt the reliability of the relativistical extended Ashley model for such a comparison as well.

5. Dynamics

The model described sofar is a static one and applies to amorphous matter. To describe the (110) channeling which is a dynamic process, the scattering of the positrons at the screened atoms and electrons must be considered. How this dynamical process can be included into the model has been described in detail in [5] for diamond single crystals and electron channeling. The formalism can be adapted also for positron channeling, however, special care has to be taken on the positron electron interaction since it is for deeply bound channeled positrons the dominating process. In order to proceed further, the electron density and the positron–electron cross-sections must be known both as function of the interplanar coordinate x.

5.1. Decomposition of the electron density across the transverse (110) channel

It can be seen from Fig. 7(a) that for positron channeling the electron distribution $n_e(x)$ peaks at $x = \pm d_p/2$, i.e. at the position where the atomic density is largest. It can be seen further that the density approaches a constant value at $x = 0$, and in addition, that the assumption of a mean value $\overline{n_e(x)}$ for the electron density across the channel would be extremely poor. It is obvious that the peak structure originates from the atomic core of the silicon atom with closed K- and L shells, i.e. a Ne-like structure, while the remaining outer four M electrons which form the valance band are unbound. The latter are of crucial importance since they are responsible for the plasmon resonances with huge cross sections, as shown in Figs. 4 and 5. In principle, quantum mechanical calculations are required to obtain the wanted densities across the channel. However, this is bejond the scope of this paper and the following is based on model assumptions. In lowest order it will be assumed that the valence electron distribution is a constant across the channel with $n_e^{val}(x) = 4/14\ \overline{n_e(x)}$. The core distribution would be in this case $n_e^{core}(x) = n_e(x) - 4/14\ \overline{n_e(x)}$. This is already a rather good approximation as can be seen from Fig. 7(a). However, it turns out that the mean value $\overline{n_e(x)} = 0.020/\mathring{A}^3$ is slightly larger than $n_e(0) = 0.185/\mathring{A}^3$ at $x = 0$. As a consequence, either the functional core or the valence electron density, or both, must be slightly adjusted. Adjusting only the core electron density by a function $g(x)$, with the side condition $\overline{g(x)} = 0$, which takes away density for x close to zero and redistributes it to $\pm d_p/2$, cures the problem.

5.2. Decomposition of cross-section

The total energy differential cross-section is shown in Fig. 5. As already mentioned, two domains can clearly be recognized which are separated by the L edge at 99.2 eV. The low energy part is the plasmon region which originates from the four "dissolved" M electrons, the high energy part, the inner-shell excitation region, originates from the Ne-like core. It can be concluded from Fig. 5 that the dominating cross-section originates from distant collisions with energy transfers less that about 100 eV, i.e., the plasmon resonance region. In particular, in the middle of the channel around $x = 0$ the inner shell excitation is nearly absent since the density from the neon-like electron core levels off here. The cross-sections are predicted by the model and are for the plasmon region $\sigma^{val} = 4.30 \cdot 10^{-3}\mathring{A}^2$, and for the inner-shell region $\sigma^{core} = 0.88 \cdot 10^{-3}\mathring{A}^2$, with total cross section $\sigma^{tot} = 5.17 \cdot 10^{-3}\mathring{A}^2$. Due to the lack of better knowledge, the differential cross-section across the channel is assumed to be a constant as shown in Fig. 7, lower part.

The simulation procedure follows the scheme described in [5, Chapter 2]. For the movement of a particle at position x_k with transverse energy $E_{\perp,k}$ to $x_{k+1} = x_k + \Delta x_k$ a time Δt_k is required which corresponds

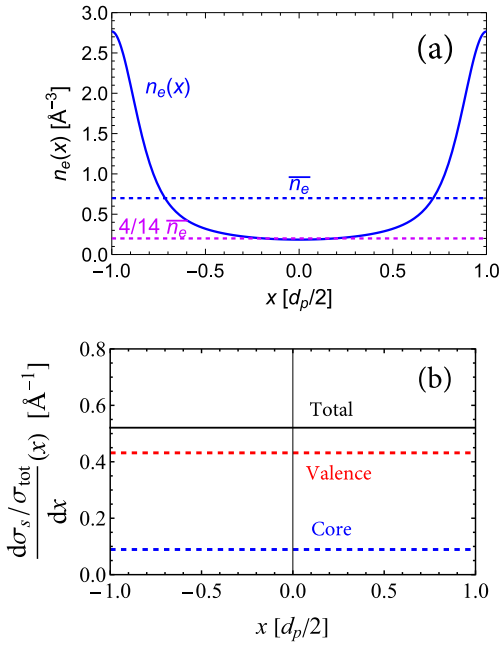

Fig. 7. Upper part: Electron density across the (110) channel which can be decomposed in a core electron and a valence electron part. For details see text. Lower panel: Model of normalized cross-sections across the channel. Red-dashed: valence electrons in the plasmon region, blue-dashed: inner-shell excitation, black: sum of both.

to a step size Δz_k in beam direction. According to the electron density at x_k and the total cross-section σ^{tot}, a collision with an electron may occur, or not. In case of a collision it will be randomly decided, on the basis of the cross-section distribution shown in Fig. 7(b), whether it was a collision with valence or core electrons. This distinction allows an investigation of the role of the plasmon resonance by switching the plasmon region in the simulation on or off. With the aid of the two dimensional cross-section shown in Fig. 4, a random momentum transfer qa_0 and energy transfer W are determined. The energy loss is directly given by the energy W, the scattering angle has been determined with Eq. 50 of [5] in which qa_0 and W enter.

Of crucial importance is a check of the assumptions for the cross-section distribution shown in Fig. 7. For off-channeling, the energy loss distribution function of Fig. 6 should be reproduced approximately. To achieve this goal, the electron density across the channel was varied with the function $g(x)$ by a trial and error method. The best result obtained is shown in Fig. 8, blue histogram.

To investigate the role of the plasmon resonances for the most probable energy loss, a low energy cut-off was introduced at 100 eV resulting in a shift of the most probable energy loss by 10 keV towards lower energies, see Fig. 8, red histogram. In other words, the plasmon region contributes to the most probable energy loss by about 25%, the remainder are from close collisions with bound K- or L-electrons. Whether these values are connected to the equipartition rule [1,23], applied by Trofymenko et al. [24], remains an open question. In case it would, the rule is in our model not fulfilled since a ratio 50 to 50 would be expected. Anyway, a precise measurement of the Landau distribution function may contribute to solve the question whether the decay of plasmon resonances occurs by electron–hole excitations, and this way contribute to the energy deposition, or rather by other channels like phonon excitations.

6. Results and discussion for positrons

6.1. Energy loss and scattering angle distributions

In an experiment the energy loss of the positrons in a silicon detector and the scattering angle can be measured simultaneously for every

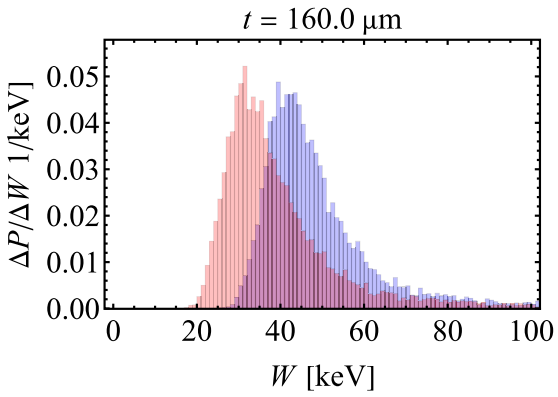

Fig. 8. Probability densities for the energy loss distribution of a 160 μm thick silicon crystal. Blue with plasmon resonances, red with cut-off at an energy of 100 eV. A number of 10,000 events were randomly distributed across the (110) channel, and the energy loss calculated with the distributions shown in Fig. 7 with adoptions described in the text.

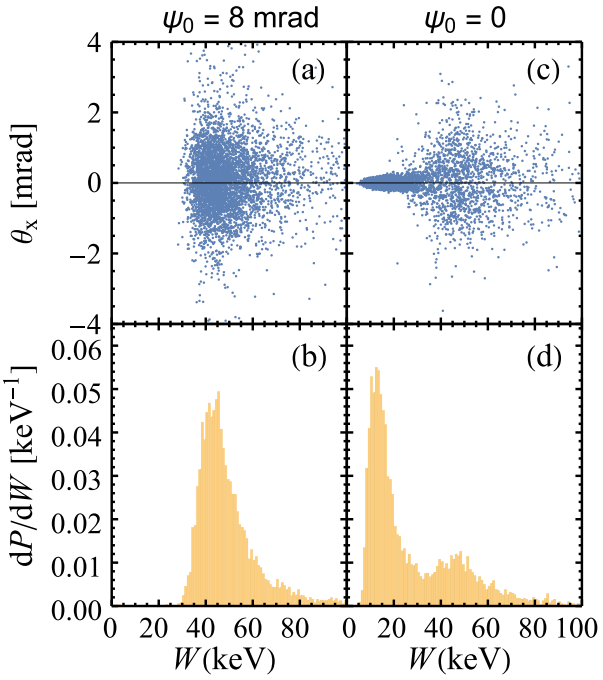

Fig. 9. Scatter plots, panels (a) and (c), and projections on the energy loss axis W, panels (b) and (d). Panels (a) and (b) represent the random, panels (c) and (d) the channeling orientation. Crystal thickness 160 μm, 5000 events were collected.

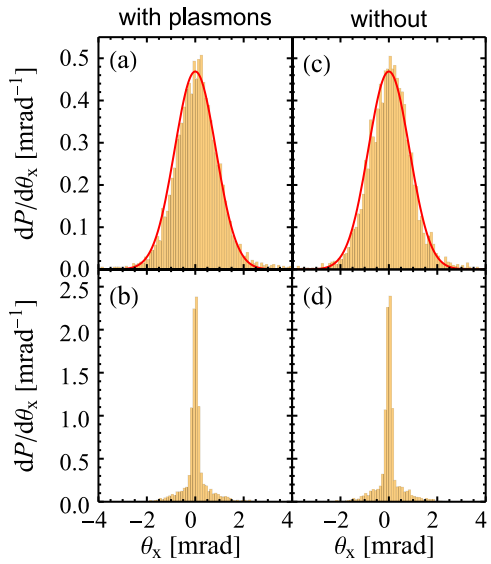

Fig. 10. Scattering angle distributions at off-channeling condition with ψ_0 = 8 mrad, panels (a) and (c), and at channeling with ψ_0 = 0 mrad, panels (b) and (d). Thickness of the crystal t = 160 μm. The red curves in panels (a) and (b) are Gaussians with the scattering distribution according to the Particle Data Group of $\sigma_{PD} = 8.512 \cdot 10^{-4}$ rad.

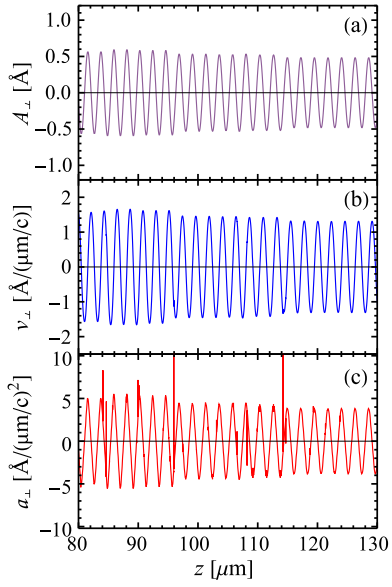

Fig. 11. Transverse characteristics of a channeling trajectory. (a) Amplitude, (b) transverse velocity and (c) transverse acceleration.

event. Fig. 9, left panels, show scatter plots for the detector oriented randomly, i.e. de-tuned to ψ_0 = 8 mrad with respect to the channeling direction, and in the right panels at channeling with ψ_0 = 0. For the latter a large fraction of events features low energy loss and little scattering. These are 3331 out of 5000 events which remain in the channel all the way to the exit of the crystal. It appears that these events form also a Landau-like distribution with a lower most probable energy loss of 17 keV. In case the positron suffers de-channeling, the energy loss and the scattering angle resemble both that of the randomly oriented crystal.

If the plasmon resonance region is turned off by a low energy cut-off in the energy loss W at 100 eV, significant shifts were recognized for the energy loss distribution (not shown here). However, as demonstrated in Fig. 10, the projected scattering distributions are virtually the same. Even the number of events that remain in the channel is within statistics the same: 3330 out of 5000, without plasmons taken into account, and 3331 out of 5000, with plasmons.

This finding suggests that scattering, and also de-channeling, is essentially governed by collisions of the positrons with atoms, including bound electrons, rather than plasmons.

6.2. Spectral power density analysis

At channeling in a deeply bound state the positron moves through the crystal with only little interaction with electrons comprising the crystal, and a quite regular transverse oscillation is expected. As an example, Fig. 11 shows amplitude, transverse velocity and acceleration, in panels (a), (b) and (c), respectively. A scattering process changes the derivative of the trajectory, and, in particular, the acceleration. This manifests itself in Fig. 11(c) by the spices.

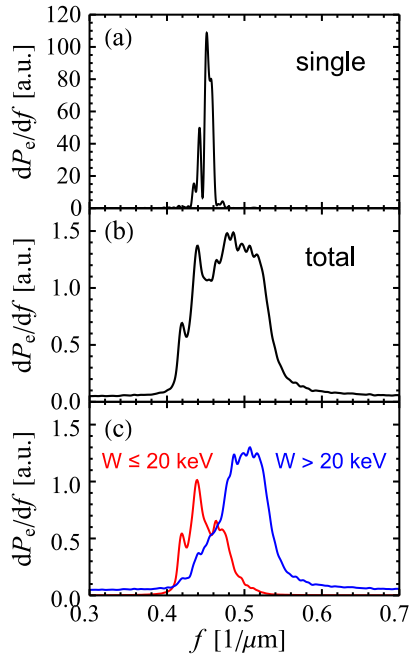

Fig. 12. Spectral power densities for positrons, panel (a) for a single trajectory, (b) the mean for 2000 single trajectories, and (c) decomposed spectra according to windows in Fig. 9(d) below and above 20 keV. Formally, f transforms in an energy scale like $\hbar\omega = 2\gamma^2\hbar c\ 2\pi f/(1+\gamma^2\theta^2$.

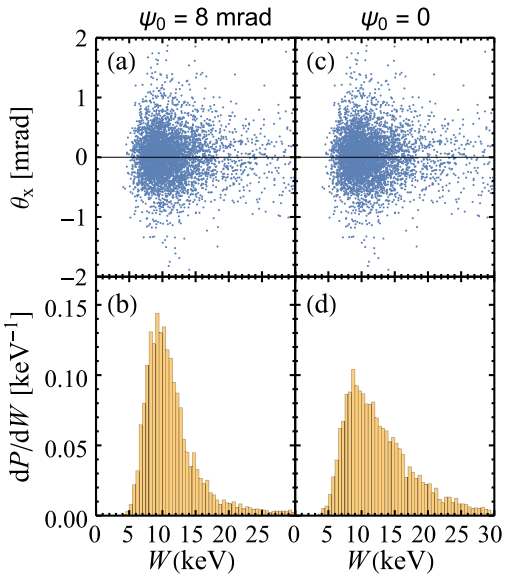

Fig. 13. Scatter plots, panels (a) and (c), and projections on the energy loss axis W, (b) and (d), for 500 MeV electrons. Panels (a) and (b) depict the random situation, (c) and (d) for channeling. Crystal thickness t = 40 μm, 5000 events.

To get an idea on the emitted spectra, in Fig. 12(a) the power density spectrum of a complete single trajectory is shown as calculated with the function PowerSpectralDensity of the Mathematica 13.2 package. Assuming that this power density spectrum shifts relativistical in forward direction like in an undulator, the transformed energy reads

$$\hbar\omega = k\frac{4\pi\gamma^2\hbar c}{\lambda_U(1+K^2/2+\gamma^2(\theta_x^2+\theta_y^2))}. \tag{5}$$

In lowest order $k = 1$, $\theta_x = \theta_y = 0$, amplitude A = 0.5 Å, period λ_U = 2.04 μm, undulator parameter $K = \gamma \cdot A \cdot 2\pi/\lambda_U$ = 0.14 one obtains $\hbar\omega$ = 1.16 MeV.

In reality, many of such spectra with various amplitudes and periods superimpose. The mean of 2000 trajectories is depicted in Fig. 12(b). The two features at 0.42 and 0.44 /μm are not statistical artifacts. They appear more clearly in panel (c) in which the mean spectrum in (b) was subdivided by windows in the energy loss spectrum shown in Fig. 9(d) into two parts. A clear effect by the chosen energy window below and above 20 keV can be stated. The origin of the structures around 0.44/μm is not quite clear. Probably they may reflect deviations from the harmonic potential. However, it should be mentioned that the spectral distribution may be broadened by incoherent processes like the collision broadening which is not invoked in the results presented in this work. Such effects were discussed in connection with experimental observations, see e.g. [25], in a number of publications in the 80s and 90s of the last century, see in particular the articles of Andersen et al. [26] and Dabagov et al. [27]. Both aspects, structure and collision broadening, may open novel insights into the channeling process of ultra-relativistic leptons treated in this paper classically.

7. Results and discussion for electrons

Although not the main aim of this work, in the following some results for electrons will be presented. The simulations were performed for a somewhat thinner crystal of 40 μm since the de-channeling length for electrons is smaller than for positrons. A beam with an emittance of ϵ_v = 0.003 π mm mrad (1 σ) in vertical direction can be provided by MAMI. An angular spread of 71 μrad (FWHM) and a beam width of 0.236 mm (FWHM) were assumed. Contrary to positrons, electrons channel in a region with enhanced electron density in the middle of the channel. Consequently the energy loss increases in comparison to positron channeling. The equivalent of Fig. 9 for positrons is shown for electrons in Fig. 13. Although no peak can be observed in Fig. 13(d), the effect of an enhanced energy loss can clearly be recognized by a comparison with the random case panel (b) which exhibits a decrease at the maximum in favor of a shoulder at the high energy side.

In Fig. 14 scattering distributions of the channeled electron are compared with the distribution for the random case. The distribution for the channeling case appears to be somewhat broader. This is expected because of the enhanced overlap of the trajectory with atoms comprising the (110) plane, and therefore enhanced scattering at atoms.

Fig. 15 depicts an electron trajectory, together with transverse velocity and acceleration. The shown de- and re-channeling characteristics turns out to be a quite general feature, which in thicker crystals may repeat itself a number of times. Fig. 15(b) indicates above barrier channeling at which the electron hobbles above the channels and still feels the potential. The velocity and acceleration frequency is increased at least by a factor of two. For electrons much more scattering processes happen in comparison to positrons. Depicting also the spikes would render the viewgraph quite confusing. Therefore the acceleration part is represented by dots for which only a few are shown in the chosen vertical scale.

Fig. 16 shows power density spectra. The single spectra are broad, and consequently also their means over many trajectories. The channeling radiation spectrum shifts to about twice the energy in comparison to positrons, however, is rather broad. An effect of an energy loss selection for electrons is less pronounced than for positrons. A window for the energy loss region 11 keV < W < 20 keV exhibits no clear discrimination in comparison to the total spectra, or the "remainder" part not in this window.

A surface barrier detector allows to change the sensitive layer by the reverse bias. In Fig. 17 the effect for different sensitive thicknesses for a 60 μm thick crystal is shown. At entrance of the electron at channeling condition ψ_0 = 0 mrad is even for a thickness of 60 μm still higher than for the off-channeling condition ψ_0 = 8 mrad. This finding may be interpreted as to originate from re-channeling which cannot

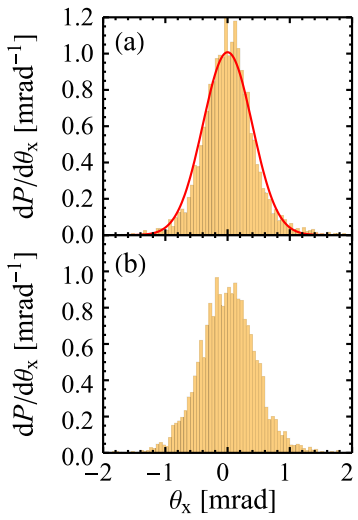

Fig. 14. Scattering angle distributions at off-channeling condition for 500 MeV electrons with ψ_0 = 8 mrad ("random"), panel (a), and at channeling with ψ_0 = 0 mrad, panel (b). Thickness of the crystal t = 40 μm. The red curve in panel (a) is a Gaussian with the scattering distribution according to the Particle Data Group of $\sigma_{PD} = 3.96 \cdot 10^{-4}$ rad.

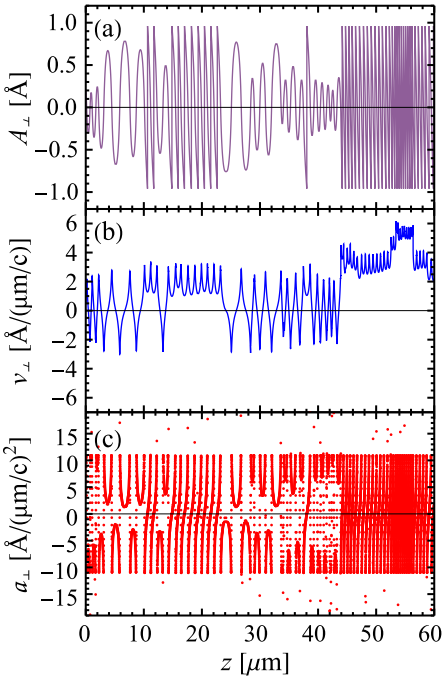

Fig. 15. Transverse characteristics for an electron channeling in a 60 μm thick crystal. Part (a) shows the amplitude, (b) the transverse velocity, and (c) the transverse acceleration.

be neglected even at those thicknesses. It is somewhat surprising that at small sensitive thicknesses an expected strong change of the energy loss seems to be absent. This effect may originate from a rapid first de-channeling. It remains an open question which information on the de-channeling process can be extracted from a measurement without employing a model for the analysis.

8. Conclusions

Simulation calculations were performed for 500 MeV positrons and electrons channeling in silicon single crystals. In particular, three quantities were investigated which can be measured simultaneously event by

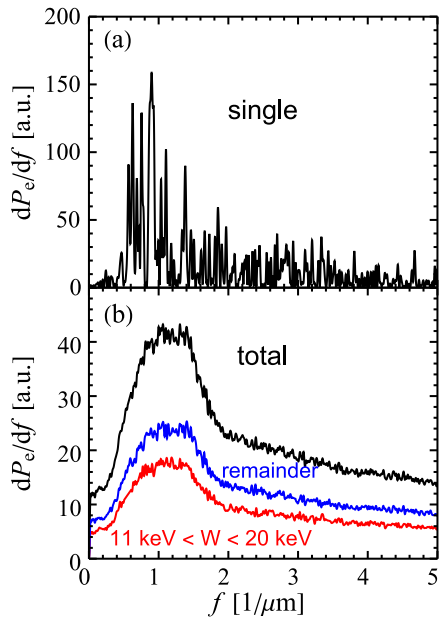

Fig. 16. Spectral power densities for electrons. Panel (a) shows a spectrum for a single trajectory, panel (b) the mean for 1500 single trajectories in black, and decomposed spectra with windows in Fig. 13 in the energy loss region 11 keV < W < 20 keV in red color, and the remainder of the spectrum in blue color. Formally, f transforms in an energy scale like $\hbar\omega = 2\gamma^2\hbar c\ 2\pi f/(1+\gamma^2\theta^2)$.

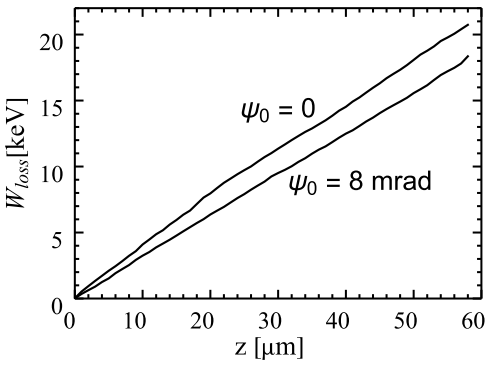

Fig. 17. Energy loss as function of the sensitive thickness for a 60 μm thick detector at channeling ψ_0 = 0, and in random orientation ψ_0 = 8 mrad.

event. These are the scattering angle, the emitted photon energy and the energy loss in the crystal if designed as a surface barrier detector. One of the main questions of this case study was to investigate the impact of the strong plasmon resonances below 17 eV. It was found that they have impact on the energy loss distribution but not the angular ones. By windows on the energy loss spectra the spectral distribution may be narrowed. However, any kind of collision broadening was not considered in this case study. Anyway, both effects may be of interest to understand better the features of the channeling process.

The main shortcoming of the simulation calculations are crude model assumptions in Section 5.1 "Decomposition of the electron density across the transverse (110) channel" made for the density distribution and the interaction cross-section of the relativistic lepton at interactions with lattice electrons, both as function of the interplanar distance x. To overcome them, quantum mechanical calculations for these quantities are needed. However, the author hopes that the estimates presented in this paper may be of some use to plan experiments at the 500 MeV positron beam under construction at the Mainz Microtron MAMI.

Declaration of competing interest

The authors declare that they have no known competing financial interests or personal relationships that could have appeared to influence the work reported in this paper.

Data availability

All data are freely available.

Acknowledgments

I would like to express my gratitude to José M. Fernández-Varea to provide me with numerical data of H. Bichsel [18] for the optical oscillator strength (OOS) of silicon.

Fruitful discussions with W. Lauth, G. Kube, A.V. Shchagin, and A. V. Solov'yov are gratefully acknowledged.

Funding

This work has been financially supported by the European Innovation Council (EIC) Pathfinder TECHNO-CLS project 101046458.

References

[1] J. Lindhard, Influence of crystal lattice on motion of energetic charged particles, Mat. Fys. Medd. Dan. Vid. Selsk. 34 (14) (1965) 1–64.

[2] A.V. Korol, G.B. Sushko, A.V. Solov'yov, All-atom relativistic molecular dynamics simulations of channeling and radiation processes in oriented crystals, Eur. Phys. J. D 75 (2021) 107, http://dx.doi.org/10.1140/epjd/s10053-021-00111-w.

[3] E. Bagli, V. Guidi, DYNECHARM++: A toolkit to simulate coherent interactions of high-energy charged particles in complex structures, Nucl. Instrum. Methods Phys. Res. B 309 (2013) 124–129, http://dx.doi.org/10.1016/j.nimb.2013.01.073.

[4] A. Sytov, V. Tikhomirov, L. Bandiera, Simulation code for modeling of coherent effects of radiation generation in oriented crystals, Phys. Rev. Accelerators Beams 22 (2019) 064601–064610, http://dx.doi.org/10.1103/PhysRevAccelBeams.22.064601.

[5] H. Backe, De-channeling in terms of instantaneous transition rates: computer simulations for 855 MeV electrons at (110) planes of diamond, Eur. Phys. J. D 76 (2022) 153–168, http://dx.doi.org/10.1140/epjd/s10053-022-00464-w.

[6] H. Backe, Beam steering with quasi-mosaic bent silicon single crystals: computer simulations for 855 MeV and 6.3 GeV electrons and comparison with experiments, Eur. Phys. J. D 76 (2022) 143–152, http://dx.doi.org/10.1140/epjd/s10053-022-00463-x.

[7] A. Shchagin, G. Kube, S. Strokov, W. Lauth, Surface-barrier detector with smoothly tunable thickness of depleted layer for study of ionization loss and dechanneling length of negatively charged particles channeling in a crystal, 2022, pp. 1–9, http://dx.doi.org/10.48550/arXiv.2211.01913, arXiv:2211.01913v2 [physics.ins-det].

[8] H. Backe, W. Lauth, P. Drexler, P. Heil, P. Klag, B. Ledroit, F. Stieler, Design study for a 500 MeV positron beam at the mainz microtron MAMI, Eur. Phys. J. D 76 (2022) 150, http://dx.doi.org/10.1140/epjd/s10053-022-00465-9, 10.

[9] G. Molière, Theorie der streuung schneller geladener Teilchen I, Einzelstreuung am abgeschirmten Coulomb-feld, Z. Naturforsch. 2 a (1947) 133–145.

[10] K. Chouffani, H. Überall, Theory of low energy channeling radiation: Application to a germanium crystal, Phys. Status Solidi (b) 213 (1999) 107–151.

[11] P.A. Doyle, P.S. Turner, Relativistic Hartree–Fock X-ray and electron scattering factors, Acta Crystallogr. A 24 (1968) 390–397.

[12] [link]. http://www.ioffe.ru/SVA/NSM/Semicond/Diamond/basic.html.

[13] V.N. Baier, V.M. Katkov, V.M. Strakhovenko, Electromagnetic Processes at High Energies in Oriented Single Crystals, World Scientific, World Scientific Publishing Co. Pte. Ltd, P O Box 128, Farrer Road, Singapore 912805, Singapore, New Jersey, London, HongKong, 1998.

[14] V.F. Sears, S.A. Shelley, Debye–Waller factor for elemental crystals, Acta Crystallogr. A 47 (1991) 441–446.

[15] J.C. Ashley, Energy-loss probabilities for electrons, positrons, and protons in condensed matter, J. Appl. Phys. 69 (1991) 674–678, http://dx.doi.org/10.1063/1.347348.

[16] B. Henke, E. Gullikson, J. Davis, X-ray interactions: photoabsorption, scattering, transmission, and reflection at E=50–30000 eV, Z=1-92, At. Data Nucl. Data Tables 54 (1993) 181–342.

[17] [link]. https://henke.lbl.gov/optical_constants/asf.html.

[18] H. Bichsel, Straggling in thin silicon detectors, Rev. Modern Phys. 3 (1988) 663–699.

[19] J.M. Fernández-Varea, F. Salvat, M. Dingfelder, D. Liljequist, A relativistic optical-data model for inelastic scattering of electrons and positrons in condensed matter, Nucl. Instrum. Methods Phys. Res. B 229 (2005) 187–218, http://dx.doi.org/10.1016/j.nimb.2004.12.002.

[20] [link]. https://physics.nist.gov/PhysRefData/Star/Text/ESTAR.html.

[21] [link]. https://physics.nist.gov/PhysRefData/XrayMassCoef/tab1.html.

[22] D. Hoffmann, C. Brendel, H. Genz, W. Löw, S. Müller, A. Richter, Inner-shell ionization by relativistic electron impact, Z. Phys. A 239 (1979) 187–201.

[23] J. Lindhard, A. Winther, Stopping power of electron gas and equipartition rule, Mat. Fys. Medd. Dan. Vid. Selsk. 34 (4) (1964) 1–22.

[24] S. Trofymenko, I. Kyryllin, On the ionization loss spectra of high-energy channeled negatively charged particles, Eur. Phys. J. C 80 (2020) 689, http://dx.doi.org/10.1140/epjc/s10052-020-8127-z, 6.

[25] J. Andersen, E. Bonderup, R. Pantell, Channeling radiation, Ann. Rev. Nucl. Part. Sci. 33 (1983) 433–504.

[26] J. Andersen, E. Bonderup, E. Læ gsgaad, A. Sø rensen, Incoherent scattering of electrons and linewidth of planar-channeling radiation, Phys. Scr. 28 (1983) 308–330.

[27] S.B. Dabagov, V.V. Beloshitsky, M.A. Kumakhov, Planar-channeling radiation from MeV electrons in diamond and silicon, Nucl. Instrum. Methods Phys. Res. B 74 (1993) 368–374.